A Geodynamic Investigation of Plume-Lithosphere Interactions Beneath the East African Rift

Tahiry A. Rajaonarison[1,2]*, D. Sarah Stamps[1], John Naliboff[2,3], Andrew Nyblade[4], Emmanuel A. Njinju[1]

[1]Department of Geosciences, Virginia Tech, Blacksburg, VA, USA
[2]Department of Earth and Environmental Sciences, New Mexico Tech, Socorro, NM, USA
[3]Department of Earth and Planetary Sciences, University of California, Davis, CA, USA
[4]Department of Geosciences, Pennsylvania State University, State College, PA, USA

*Corresponding author: Tahiry A. Rajaonarison (tahiry.a.rajaonarison@gmail.com)

Key Points:

- Geodynamic modeling suggests observed rift parallel motions influenced by the African Superplume
- Asthenospheric seismic anisotropy induced by northward flow associated with the African Superplume
- Horizontal mantle tractions driving surface deformation

Abstract

Constraining the origin of forces that drive continental rifting remains a highly debated and unresolved question within geodynamics. The East African Rift (EAR) provides an ideal natural laboratory to examine the relative role of plate driving forces as only lithospheric buoyancy forces and horizontal mantle tractions act on the system. Here, we employ high-resolution 3D thermomechanical models to test whether: 1) anomalous, rift-parallel surface deformation observed by GNSS data in the EAR are driven by viscous coupling to northward mantle flow associated with the African superplume, and 2) the African superplume is the dominant source mechanism of anomalous rift-parallel seismic anisotropy beneath the EAR. We calculate Lattice Preferred Orientations (LPO) and surface deformation from two types of mantle flow: (1) a scenario with multiple plumes constrained by shear wave tomography and (2) a single superplume model with northward boundary condition to simulate large-scale flow. Comparison of calculated LPO with observed seismic anisotropy, and surface velocities with GNSS and plate kinematics reveal that there is a better fit with the superplume mantle flow model, rather than the tomography-based (multiple plume) model. We also find a relatively better fit spatially between observed seismic anisotropy and calculated LPO with the superplume model beneath northern and central EAR, where the superplume is proposed to be shallowest. Our results suggest that the viscous coupling of the lithosphere to northward mantle flow associated with the African superplume drives most of the rift-parallel deformation and is the dominant source of the observed LPO in the EAR. The model show that northward mantle flow associated with the African superplume drives most of the rift-parallel deformation in the EAR and is the dominant source of the observed LPO in the EAR.

Plain Language Summary

What forces drive continental rifting remains an outstanding question of geodynamics. During continental rifting, surface deformation and the underneath mantle flow are usually perpendicular to the rift. In the case of the East African Rift (EAR), the largest continental rift on Earth, it has been demonstrated that its E-W extension is mostly driven by forces due to its high-topography, but some deformations are parallel northward to the rift. Here, we use 3-dimensional computer simulation to test if these anomalous deformations are driven by hot buoyant upwelling known as African Superplume. Comparison of model results with measured surface deformation, measured with highly accurate Global Position System (GPS) measurements, show that mantle northward associated with the African Superplume drive some of the rift parallel deformations in the EAR. Our results also suggest that most of the enigmatic rift parallel seismic anisotropy, nowadays observed by geophysicist beneath the EAR, can be explained by the large northward mantle flow from the African Superplume.

1. Introduction

Continental rifting is an important geodynamic process during which the Earth's lithosphere undergoes continuous stretching resulting in continental break-up and, ultimately, the formation of new oceanic basins. In the past few decades, many geophysical studies have been carried out to elucidate the driving forces of continental rifting in order to advance our understanding of rift initiation and evolution (e.g. Mulugeta, 1985; Buck, 1991; Brune, 2018; Glerum et al., 2020; Naliboff et al., 2020). The origin of extensional stresses responsible for continental rifting can be classified into two categories: 1) horizontal tractions at the base of the lithosphere arising from mantle convection (Froidevaux and Nataf, 1981; Lithgow-Bertelloni and Guynn, 2004; Bird et al., 2008; Forte et al., 2010; Ghosh and Holt, 2012) and 2) variations in lithospheric buoyancy forces arising from topography gradients and density variations (e.g. Bott and Kusznir, 1979; Lithgow-Bertelloni and Silver, 1998; Coblentz and Sandiford, 1994; Lithgow-Bertelloni and Guynn, 2004; Ghosh et al., 2009; Naliboff et al., 2012; Stamps et al., 2014, 2015; Rajaonarison et al., 2021a).

The EAR is region of continental extension within the diverging the Nubia-Somalia plate system, with kinematic models derived from GPS data suggesting an ~E-W extension direction (Calais et al., 2006; Saria et al., 2014; Stamps et al. 2021; Figure 1.1A). Previous studies suggest E-W extension of the EAR is driven largely by lithospheric buoyancy forces attributed mainly to the unusually high topography (higher than 1000 m above sea level) known as the African Superswell (e.g., Nyblade and Robinson, 1994) of the EAR (Figure 1.1A) and to density variations within the lithosphere (e.g. Coblentz and Sandiford, 1994; Stamps et al., 2014, 2015; Rajaonarison et al., 2021a). However, other studies propose horizontal mantle tractions drive a significant portion of the E-W extension in Africa (e.g. Ghosh and Holt, 2012; Kendall and

Lithgow-Bertelloni, 2016). Significantly, all of the aforementioned studies approximate deformation within the lithosphere using a depth-independent 2D (i.e., thin shell or sheet) modeling approach. In contrast, recent 3D thermomechanical modeling (Rajaonarison et al., 2021a) suggests that the E-W extension of the EAR, (i.e., the rigid plates and microplates rotation and their velocity magnitudes) is dominated by lithospheric buoyancy forces and that additional forces, such as viscous coupling to mantle flow, are only needed to explain the anomalous observed northward surface motions within the deforming zones as revealed by GNSS/GPS velocities (Figure 1.1A, Stamps et al., 2018) and strike-slip focal mechanisms observed along multiple branches of the rift (Figure 1.1B; Dziewonski et al., 1981; Ekström et al., 2012).

Here, we expand on the work of Rajaonarison et al. (2021a) to test if plume-lithosphere interactions are a plausible explanation for the rift-parallel deformation observed along the EAR, where plume-lithosphere interactions have been suggested to be important in the system's long-term evolution and dynamics (Koptev et al., 2016; Koptev et al., 2018a, b; Koptev, Calais et al., 2018). Numerous seismic tomography studies have imaged low velocity anomalies beneath the EAR and associated them with the presence of one or more upwelling thermal anomalies (e.g., Ebinger and Sleep, 1998; Montelli et al., 2006; Hansen et al., 2012; Bagley and Nyblade, 2013; Emry et al., 2019; Chang et al., 2011, 2020). However, interpretations of these low velocity anomalies in terms of plume structure remain controversial, with two main end-member plume models (Figure 1C, D) often invoked. The first model attributes the low velocity anomalies beneath the EAR as originating from multiple plumes (Figure 1C) beneath the EAR (e.g., Camp and Roobol, 1992; Chang and Van der Lee, 2011; Ebinger and Sleep, 1998; George et al., 1998; Montelli et al., 2006). The second model invokes the African superplume (Figure 1D), which consists of a large single low velocity anomaly that penetrates the transition zone (Hansen et al., 2012), originating from the core-mantle boundary beneath South Africa with upward and northeastward flow beneath east Africa to Arabia (e.g. Bastow et al., 2008; Benoit et al., 2006; Forte et al., 2010; Furman et al., 2006; Ritsema et al., 1999; Simmons et al., 2007, 2009). The hypothesized northeastward direction of the mantle flow associated with the African superplume is supported by consistent rift-parallel (NE-oriented) shear wave splitting measurements beneath the EAR (Figure 1B; Bagley and Nyblade, 2013; Andriampenomanana et al., 2021). Bagley and Nyblade (2013) suggest that the NE-oriented azimuthal anisotropy is sourced from asthenospheric Lattice Preferred Orientation (LPO) of olivine induced by northeastward mantle flow associated with the African superplume.

In this work, we test the hypotheses that: 1) the observed northward component of surface motion is driven by viscous coupling between the lithosphere and northward mantle flow beneath the EAR, and 2) NE oriented azimuthal anisotropy beneath the EAR reflects northeastward mantle flow associated with the African superplume. To test these hypotheses, we use the open-source finite element code Advanced Solver for Problems in the Earth's ConvecTion (ASPECT) (Bangerth et al., 2015, 2020; Kronbichler et al., 2012; Heister et al., 2017) to simulate 3D convection and deformation of the lithosphere-asthenosphere system for the EAR and surroundings. Our numerical experiments build upon the model from Rajaonarison et al. (2021a), in which the deformation is driven by lithospheric buoyancy forces.

We incorporate sublithospheric mantle flow using thermal anomalies derived from the conversion of shear wave tomography from Emry et al. (2019) to account for plume structures in the upper 660 km. This shear wave model is used to represent a "multiple plumes" scenario, as it contains multiple distinct thermal anomalies rather than a single large thermal anomaly (i.e., superplume) . A second numerical experiment builds on this model by adding an imposed (boundary-drive) northward mantle flow beneath 200 km depth to simulate the proposed effects of large-scale mantle flow induced by a superplume in this region. The mantle flow velocities from each simulation are used to generate synthetic seismic anisotropy, which is compared with observed azimuthal anisotropy from the EAR region. The synthetic seismic anisotropy is calculated using D-Rex (Kaminski et al., 2004), which follows the kinematic model for plastic deformation and dynamic recrystallization (Kaminski and Ribe, 2001, 2002; Ribe and Yu, 1991). To assess the influence of mantle flow on surface deformation, we quantitatively compare surface motion from both models with GNSS observations from Stamps et al. (2018) and block kinematic models from Stamps et al. (2021).

We find that the presence of multiple plumes or the superplume does not affect the rigid block rotation of the Victoria and Rovuma Blocks, but produces faster velocities (up to twice in velocity magnitude) for the Somalian Plate. We also find that the northward component of motion along the Main Ethiopian Rift, the Western Branch, and the central Eastern branch can be explained by viscous coupling of the lithosphere to northward mantle flow associated with the African Superplume. The velocity angular misfit between predicted velocities and GNSS/GPS observations in these regions improve from 66° , 114° , and 74° , respectively from a model with deformation driven solely by lithospheric buoyancy forces (Rajaonarison et al., 2021a), to 50° , 40° , and 30° , respectively. This improvement of the angular misfit suggests that viscous coupling to northward mantle flow is favored within the deforming zones. Our results also suggest that additional mechanisms, such as anisotropic viscosity in the asthenosphere is needed to explain the rotation rate of the Somalian Plate. Although lithospheric buoyancy forces dominate the force balance driving E-W extension across the EAR, this work suggests horizontal tractions from northward mantle flow associated with the African Superplume is needed to explain observations of rift-parallel surface motions in deforming zones from GNSS/GPS data and northward oriented seismic anisotropy beneath the EAR.

2 Methods

2.1 Model Design and Experiments

We use the finite element code ASPECT (Advanced Solver for Problems in Earth's ConvecTion; Heister et al., 2017; Kronbichler et al., 2012), which has been widely employed to investigate melt/mantle dynamics (Dannberg et al., 2019; Dannberg & Heister, 2016; Njinju et al., 2021), lithospheric deformation and continental extension (Glerum et al., 2020; Naliboboff et al., 2020), and global/regional mantle convection (Rajaonarison et al., 2020; Zhang & Li, 2018), to simulate lithospheric deformation and mantle flow within the EAR region. Surface and internal velocities are calculated with Stokes system of equations, which follows the Boussinesq approximation for an incompressible Newtonian fluid. Although the aim of this study is to assess the contributions of horizontal tractions from mantle flow beneath the EAR, it is important that the primary driving forces acting in this region, which are lithospheric buoyancy forces and horizontal mantle tractions, are incorporated in the model. Thus, our model is derived from Rajaronarison et al. (2021a,b) in which the lithospheric buoyancy forces are implemented using ETOPO1 (Amante and Eakins, 2009) for the surface topography, CRUST1.0 for the laterally varying crustal structures and densities (lower, middle, and upper crust; Laske et al., 2013), and isostatically compensated to 100 km depth for the mantle lithosphere density.
Here, mantle flow fields driven by density heterogeneities are added in the sublithospheric regions. The sublithospheric mantle densities in our simulations vary linearly with temperature:

$$\rho = \rho_0(1 - \alpha(T - T_0) \quad (1.1)$$

where α is the thermal expansion coefficient. The Stokes and temperature system of equations is solved within a 3D spherical chunk geometry model domain, covering 5300×3300×660 km in the East, North, and radial directions, respectively.

The initial temperature structure throughout the lithosphere is calculated following the approach of Chapman (1986), which uses an analytical solution for a conductive geothermal profile to obtain temperatures throughout a layered lithosphere (upper crust, middle crust, lower crust, and mantle lithosphere). A key assumption to this approach is that each layer contains a constant thermal conductivity and radiogenic heat production, unique for each layer (Table B.1). While the lithosphere-asthenosphere boundary is defined by the 1673 K isotherm, the lithospheric geothermal gradient varies as a function of lithospheric thickness, the surface heat flow, and the crustal thicknesses (CRUST1.0). We use lithospheric thicknesses that capture the key tectonic regions obtained from averages of the lithospheric models LITHO1.0 Pasyanos (2013), Fishwick (2010, updated), and Emry (per comm.). For the cratonic regions, including the Tanzania Craton, the Congo Craton, the Bangweulu Block, and the Masai Block, the lithospheric thicknesses are 150 km thick. The Eastern Branch and the Western Branch of the EARS have 70 km and 90 km thick lithosphere, respectively. We impose 50 km lithosphere thickness for oceanic ridges. We also assume a 100 km thick lithosphere for mobile melts, and for the oceanic lithosphere, and other regions not previously defined.

In sub-lithospheric regions, the temperature is the sum of an approximate adiabatic temperature profile (with 0.3 K/km increase with depth; Schuberth et al., 2009) and a temperature anomaly obtained using a conversion of shear wave anomalies from Emry et al. (2019), which is shown in Figure 3A,B. We choose a simple approach for the conversion of shear wave velocities to temperature to minimize complexity in the model. The shear wave anomalies are first converted to density perturbations $\delta\rho/\rho$ using a velocity-density factor of 0.15 following numerous previous studies (e.g., Becker, 2006; Conrad and Lithgow-Bertelloni, 2006; Conrad and Behn, 2010). The density perturbation is further translated into a temperature anomaly ΔT (Figure 2C, D) by multiplying it by the negative inverse of thermal expansion (e.g., Austermann et al., 2017; Karato, 1993). The shear wave tomography from Emry et al. (2019) shows low velocities up to 6-12% beneath the Kenya Rift and the Main Ethiopian Rift (Figure 2A, B), which could result in a temperature excess of 500-1000 K following the conversion outlined method above. However, these temperatures are higher than typical excess plume temperatures ranging from 200-300 K (e.g., Schuberth et al., 2009). We therefore apply a temperature excess cut-off of 300 K during the shear wave anomaly to temperature conversion. This assumption is supported by geochemical evidence suggesting that low seismic shear wave velocities beneath the EAR are a combined contribution from mantle temperature, melt (at shallow depth), and composition beneath 200 km (Rooney et al., 2012). Details of the calculation of our lithospheric geothermal gradient is described in the Supplementary material.

The numerical experiments incorporate non-linear (non-Newtonian) rheological flow laws, which are needed to match first-order observations of solid Earth deformation and constraints from rock deformation experiments (Figure 3). In brittle regions (i.e., in the upper crust and uppermost mantle), plasticity limits the stress and reduces viscosity, which we assume is in accordance with a Drucker-Prager yield criterion. The viscous flow law for the crust is visco-plastic with dry quartzite and dislocation creep for dry olivine in the mantle lithosphere. We assume that the main composition of the mantle is dry olivine since the area is far from a subduction zone. The flow in the sublithospheric mantle lithosphere is governed by composite rheology (Jadamec and Billen, 2010). A plastic strain weakening factor for cohesion and friction is applied to the lithospheric viscosity in the deforming zones (Stamps et al., 2018) in order to promote strain localization.

The velocity boundary condition at the model surface is free slip in order to minimize unrealistic vertical motions and restrict near-surface motion to be horizontal. For the multiple plumes model, the mechanical boundary conditions are free slip on all faces, except at the bottom boundary where a no-slip condition is used to simulate the relatively higher viscosity and slow mantle flow beneath the transition zone. For the superplume model, a 2 cm/yr northward velocity boundary condition is applied at the northern and southern faces below 200 km and zero velocity above this depth (See Figure 3).

2.2 Estimating Mantle Flow Induced LPO

Using the program D-Rex (Kaminski et al., 2004), we predict asthenospheric crystal aggregates LPO that develop beneath the EAR from both the multiple plume and superplume models. As D-Rex incorporates deformation mechanisms of olivine-enstatite aggregates in flow such as plastic deformation, grain boundary sliding, and dynamic recrystallization (Kaminski and Ribe, 2001, 2002), the code has been successfully used to estimate synthetic LPO that develop in response to given global or regional mantle flow fields (e.g. Faccenda and Capitanio, 2012, 2013; Hu et al., 2017; Rajaonarison et al., 2020). Since most seismic anisotropy is often interpreted as the fast axis of olivine crystals, the transverse isotropic approximation (TI) output by D-Rex is used here as a proxy for LPO (e.g., Becker et al., 2006; Faccenda and Capitanio, 2012; Hu et al., 2017). The workflow for calculating synthetic LPO that develops along pathlines in steady state flow is outlined below .

We consider particles that consist of 2000 virtual grains of olivine (70%) and enstatite (30%) crystals (Kaminski et al., 2004), which represents a harzburgite composition. The particles are located beneath the seismic stations where observations are available, and distributed between 100 km and 400 km depths with a vertical interval of 25 km. For the purpose of calculating their trajectories, first, the particles are advected backward in time, using the fourth order Runge-Kutta advection scheme described in Becker et al. (2003), during which they accumulate strain and stopped until a critical strain of 0.75 is reached (e.g., Rajaonarison et al., 2020) or until the particles reach the 410 km discontinuity. At the location where the backward advection is stopped, the particle is set with randomly oriented crystals to form an isotropic mantle and advected forward along its trajectory. During this forward advection, the mineral aggregates accumulate finite strain, LPO develops and evolves along the pathlines in response to shear. Then, D-Rex calculates the global elastic tensor of the grain assemblage using the Voigt averaging scheme for single-crystal elastic tensors and extracts the TI axis orientation that we subsequently compare with observations.

3 Results

3.1 Mantle Flow Beneath the EAR

Mantle flow from the multiple plume model is mainly characterized by localized upwelling beneath multiple rift segments of the EAR (see Figure 4). Figures 4A and 4B show map views of the multiple plumes at depth slices 150 km and 300 km, with background colors illustrating vertical velocities and the vectors indicating horizontal motions at that depth. The positive vertical velocities at 150 km (Figure 4A) indicate localized upwelling occurs beneath the Main Ethiopian Rift, the Eastern Branch, the Western Branch, and the northern Malawi Rift. The upwelling rates across the entire EAR range from 6-10 cm/yr, whereas the upwelling beneath northernmost EAR, the Main Ethiopian Rift, and Kenya Rift are more vigorous than beneath the Western Branch. These patterns of upwelling are consistent with relatively low shear wave anomalies beneath the Main Ethiopian Rift, the Eastern Branch, and northern Malawi Rift, which result in relatively higher temperature, higher buoyancy, and lower viscosity. The associated horizontal velocities show radiating patterns that result mostly in rift perpendicular flow with a dominantly E-W orientation.

At 300 km depth (Figure 4B) the horizontal velocities associated with the localized upwelling converge inward, indicating that slow seismic velocity anomalies are not connected to a deeper source that passes through the transition zone. A profile view of the mantle flow (Figure 4C) shows that the localized upwelling extends to the 410 km discontinuity and is mostly limited to that depth due to the relatively high viscosity between 410-660 km. Figure 3C also shows that a downwelling beneath the Tanzania Craton separates the upwellings beneath the Western Branch and Eastern Branch.

Asthenospheric flow from the superplume model beneath the EAR is characterized by northward horizontal flow driven by the imposed boundary velocities (Figure 5A,B). The associated vertical velocities show that the upwellings still occur beneath multiple segments of the rifts. At 150 km (Figure 5A), the northward mantle flow imposed from the southern model boundary is deflected to both the west and to the east by the rheologically strong lithosphere of the Tanzania Craton. To the west, the mantle flow is channeled northward between the Tanzania Craton and the Bangweulu Block and then accommodates the curvature of the Western Branch to the north. To the East, the mantle flow is slightly deflected eastward by the Tanzania Craton lithosphere. At 300 km depth (Figure 5B), the horizontal mantle flow mostly exhibits northward flow directions except beneath the Eastern Branch and Main Ethiopian Rift, where the horizontal flow tends to align in the ~NE direction. Figure 5C shows that beneath the thick lithosphere in the southern EAR mantle flow pattern is mostly horizontal trending northward. In contrast, beneath the thin lithosphere of northern EAR, localized upwellings still occur at shallow depths.

3.2 Comparison of Mantle Flow Induced LPO

In this section, we present the comparison of synthetic LPO, or TI-axis orientation, and observed splitting at locations where each of the observations exist (Figure 6 and Figure 7). Due to the high variability of the anisotropy orientations, we present the comparisons regionally, partitioned into northern (Region A), central (Region B), and southern (Region C) EAR. Also, given the changes of horizontal mantle flow pattern with depth from both the multiple plumes and superplume models, we illustrate and present the comparison with observations at relatively shallow asthenosphere (150 km) and at relatively deeper depths (300 km). Table 1 shows a summary of the comparison of predicted TI-axis with observed shear wave splitting. For the multiple plumes mantle flow model (Figure 6) the overall observed (N27°E) fast direction pattern (~S39°E) is poorly reproduced by the calculated synthetic LPO. At 150 km (Figure 6A), the synthetic LPO mostly exhibits a rift perpendicular trend with an average orientation of S20°E in the northern EAR (Region A), the orientation is S15°E in the central EAR (Region B), and the trend is N20°E at the southern EAR (Region C). Comparisons yield a poor angular misfit with the observations with average angular misfits of 51°, 52°, and 40°, respectively. Similarly, poor misfit are found at 300 km depth because the synthetic LPO also exhibits rift perpendicular trends with average orientations of S20°E, S15°E, and N20°E for the northern, central, and southern EAR, respectively. The corresponding mean angular misfits are 51°, 51°, and 46°, respectively. The rift perpendicular trend of the synthetic LPO is due to radiating pattern of the horizontal flow from the multiple plumes model (see Figure 4).

For the superplume mantle flow model (Figure 7), the overall observed ~NE fast direction patterns are well reproduced by the calculated synthetic LPO at relatively deeper depths (300 km; Figure 7B) than at shallow depths (150 km; Figure 7A). At 150 km (Figure 7A), the synthetic LPO mostly exhibits rift perpendicular trends (S30°E, S1°E, and N20°E, respectively, for the northern, central, and southern EAR), yielding poor mean angular misfit of 60°, 44° , and 46°, respectively. The rift perpendicular trend of the synthetic LPO at 150 km is consistent with the radiating pattern of horizontal flow pattern (see Figure 4A). At 300 km (Figure 7B), we find a good fit between the observations and the synthetic LPO with average directions of N23° E, N13°E, and N50°E for the northern, central, and southern EAR, respectively. The best fit is found in the northern EAR (Region A, Figure 7B) with an average misfit of 20◦. The angular misfits are 27° for central EAR, and 40° in the southern EAR (Region C; Figure 7B).

3.3 Surface Velocity Comparison

To test how the presence of multiple plumes or a superplume beneath the EAR drives surface deformation, we quantitatively compare our dynamic velocity estimates with kinematic predictions of surface motions within zones of rigidity (Stamps et al., 2021; Figure 1A) and GNSS/GPS velocities in intra-rift zones (Stamps et al., 2018; Figure 1A). For velocity magnitude comparison, we use the Root Mean Square velocity statistic, whereas regional mean angular misfit ([0-180] from aligned to opposite velocity direction) is used to quantify the fit between predicted and observed velocity directions. The comparison of dynamic velocities with the kinematic model and GPS observations are summarized in Table 2. Dynamic velocities driven by mantle tractions from multiple plumes mantle flow and lithospheric buoyancy forces predict well the rigid plate motions of the Victoria and the Rovuma Block with RMS misfit of 0.5 mm/yr and 0.5 mm/yr, respectively, and an angular misfit of 6◦ and 10◦, respectively (Figure 8B). For the Somalian Plate, the dynamic velocities align well with the predicted clockwise rotation with an angular misfit of 5◦, but the rotation rate is 13 mm/yr, which is three times larger than the kinematic model (4.41 mm/yr; see Table 2), resulting in a large RMS misfit of 12 mm/yr (Figure 8A). Within the deforming zones (Figure 8B), the dynamic velocities are driven by mantle tractions from the multiple plumes and lithospheric buoyancy forces resulting in a poor fit to the GNSS/GPS observations. In the MER (Region A; Figure 8), although the dynamic velocities align well with the GNSS/GPS observations at some stations within the rift, the velocities at the western border of the rift and in the southern region do not align well, yielding a mean angular misfit of 60°. The dynamic velocities are also faster, with a mean velocity of 7.1 mm/yr compared to the GNSS/GPS velocities (2.59 mm/yr; see Table 2). In the Eastern Branch (Region B,C,D; Figure 8B), we find good fits between the dynamic velocities and the GPS observations in Region B and C, with RMS misfit of 2.1 mm/yr and 1.5 mm/yr, respectively, and angular misfits of 5° mm/yr and 4 mm/yr, respectively. The fit is worse in the central Eastern Branch (Region C; Figure 8B) where the RMS misfit is 2.5 mm/yr. In Region C, the fit is consistent with some of the dynamic velocities exhibiting a ∼SE trend whereas the GPS velocities trend ∼NE, yielding poor angular misfit of 50°. For the Western Branch (Region E; Figure 8), the mean dynamic velocity magnitude is relatively small (0.2 mm/yr) compared with the 2.55 mm/yr observed by GNSS/GPS, with an RMS misfit of 1.36 mm/yr and the velocities do not align well with a poor angular misfit of 99°. For the southern EAR (Region F; Figure 8) or the northern Malawi Rift, we find a good fit of the dynamic velocities and the GNSS/GPS velocities with an angular misfit of 20° and an RMS misfit of 0.8 mm/yr. Overall, the lithospheric buoyancy forces combined with sublithospheric multiple plumes drive similar surface deformation to the lithospheric buoyancy forces alone estimated by Rajaonarison et al. (2021a,b), indicating that lithospheric deformation is decoupled from the mantle flow, except for the Somalian Plate, which appears to be coupled with the underlying eastward mantle flow.

For the model in which deformation is driven by mantle tractions from the superplume and lithospheric buoyancy forces, the block kinematics are also predicted well with angular misfits of 5°, 7°, and 6°, respectively for the Somalian Plate, Victoria Block, and Rovuma Block. Their rotation rates are slightly faster (7.5 mm/yr, 2.8 mm/yr, and 3.1 mm/yr, respectively; Figure 9A) than the kinematic model (4.41 mm/yr, 2.13 mm/yr, and 2.14 mm/yr, respectively;

Figure 9A). The Somalian Plate rotation exhibits the largest RMS misfit (5 mm/yr), indicating some degree of coupling between the plate and the underlying mantle flow. In the deforming zones, we find some improvement of the fit with the lithospheric buoyancy forces and superplume combined model. In the MER (Region A; Figure 9B), although the RMS misfit is relatively large (6 mm/yr), the mean angular misfit decreases from 66° (from the model with only GPE only, see Table 2) to 30°, with predicted velocities and observations having opposite directions at a station located in the southern part of Region A. We also find in the mean angular misfit at the central Eastern Branch (Region C; Figure 9B), where the dynamic velocities at some stations have shifted from ~SE trend to ~E-W and ~NE decreasing the mean angular misfit from 73° to 30°. In the Western Branch (Region E; Figure 9B), the mean angular misfit also significantly improves form 114° to 43° respectively. However, the dynamic velocities remain small 0.7 mm/yr compared to the GNSS/GPS velocities (2.55 mm/yr). In the southern EAR (Region F; Figure 9B), the dynamic velocities exhibit ~E-W and ~NE trends whereas the GPS velocities are oriented ~E-W and ~SE, which slightly worsens the mean angular misfit from 20° to 24°, but may be within the uncertainties of the model. Overall, the comparison of dynamic velocities from the combined lithospheric buoyancy forces and the superplume model indicates there is some degree of lithosphere coupling to northward flow, notably within the deforming zones and beneath the Somalian Plate.

4 Discussion

4.1 Source of Observed Seismic Anisotropy Beneath EAR

Overall observed seismic anisotropy in the EAR exhibits N-S or NNE trends with delay times ranging from 1-1.5 s. Most anisotropy with such relatively large delay time are often attributed to mantle flow induced LPO (Helffrich, 1995). However, in divergent settings, mantle flow induced LPO are expected to be perpendicular to the rifts. For example, along mid oceanic ridges mantle flow induced LPO are perpendicular to the plate boundaries (Becker et al., 2003, 2006, 2014). Thus, interpretations of the observed rift parallel anisotropy along the EAR remains controversial. Several mechanisms such as fossilized anisotropy due to past orogenic events (Homuth et al., 2016; Walker et al., 2004), and parallel dykes or magma filled lenses (Albaric et al., 2014; Gao et al., 1997) have been invoked as explanations for the rift parallel anisotropy. Bagley and Nyblade (2013) suggest that the overall consistent N-S or NNE trend of the anisotropy can be attributed one single mechanism that is the northward flow of the African superplume.

The results presented here corroborate with the African superplume hypothesis suggested by Bagley and Nyblade (2013) because we find good alignment with calculated LPO and observations at deeper depths (300 km) than shallower depths (150 km) for the superplume mantle flow model. Moreover, the multiple plume model does not produce a good fit with the observations indicating that mantle upwelling beneath the Main Ethiopian Rift, the Kenya Rift, the Western Branch are influenced by northward flow from the African superplume. Our results also highlight the importance of the Tanzania Craton, Congo Craton, and the Bangweulu Block in channeling the northward mantle wind resulting in rift parallel mantle flow mainly in the Western Branch. This rift parallel mantle flow results in rift parallel anisotropy explaining most of the seismic anisotropy including those in the northernmost Western Branch. It is also worth noting that sub-lithosphere mantle viscosity plays an important role in favoring rift parallel mantle flow. For example, the mantle flow and the LPO exhibit NNE trends at the Main Ethiopian Rift as a result of low viscosity along the strike of the rift.

4.2 Plume-Lithosphere Interactions Beneath EAR

Our comparison of surface velocities with predicted rigid block motion and GPS velocities highlights the importance of the interactions between the lithosphere and mantle flow associated with the African superplume beneath the EAR. The significance of plume-lithosphere interactions has been discussed by Forte et al. (2010), Ghosh and Holt (2012), and Kendall and Lithgow-Bertelloni (2016), who suggest that mantle tractions from divergent flow associated with the African superplume alone can cause the opening of East Africa. However, previous geodynamic modeling results suggest that the E-W extension of the EAR is dominated by lithospheric buoyancy forces and adding sub-lithospheric mantle flow over-predicts the observed deformation (Stamps et al., 2014, 2015). Our numerical experiments of lithospheric deformation combined with asthenospheric flow suggest that the multiple plumes model beneath the EAR does not significantly affect the surface deformation of the EAR, except for the Somalian Plate where the rotation rate is over-predicted. Moreover, the multiple plumes mantle flow cannot explain the northward component of motion with the deforming zones. The inconsistency between the multiple plume model and surface velocities in the deforming zones is likely because beneath the rifts is dominated by upwelling and diverging E-W flow beneath the adjacent rigid blocks. In contrast, the superplume model results in mantle flow beneath the rifts that is mostly oriented northward and rift parallel. This northward horizontal flow generates horizontal tractions at the base of the lithosphere and produces northward surface motions.

Our results also suggest that the counter-clockwise rotation of the Victoria Block is independent of the underlying mantle flow from the multiple plumes model, but a minor contribution might occur from the northward mantle flow associated with the African Superplume. This interpretation is consistent with the findings of Glerum et al. (2020). Due to the presence of Tanzania Craton within the Victoria Block, the lithosphere-asthenosphere coupling is expected to be significant because previous studies have shown that viscous coupling between asthenosphere and lithosphere is favorable beneath cratonic roots (Conrad and Lithgow-Bertelloni, 2006; Stoddard and Abbott, 1996; Zhong, 2001). This strong coupling is not the case for the Victoria Block possibly because of the continuation of the Congo Craton into the Tanzania Craton through the northern Western Branch (Link et al., 2010) provides resisting forces (drag) to mantle tractions. The resisting forces can be caused by the stability of the Congo Craton within the stable Nubian Plate. The role of a craton in favoring viscous coupling of mantle flow and lithosphere can, however, be observed in the central Eastern Branch, located to the north of the Masai Block. Our results indicate that due to the presence of the Masai Block, the surface deformation in the central Eastern Branch is influenced by the underlying northward mantle flow associated with the African Superplume.

4.3 Anisotropic Viscosity

Our results indicate the rotation rate of the Somalian Plate is over-predicted by our lithospheric deformation models driven by lithospheric buoyancy forces and mantle flow (multiple plumes and superplume model). Previous geodynamic modeling studies have also reported this over-prediction when coupling lithospheric deformation with basal shear from global mantle flow models (e.g., Stamps et al., 2014, 2015). These previous studies suggest that lithospheric buoyancy forces alone are capable of driving present-day plate motion of the EAR and that viscous coupling between mantle flow and lithosphere should be inefficient. Stamps et al. (2015) attribute the inefficiency of coupling with lower viscosity of the asthenosphere or slower mantle flow than is often estimated. An alternative mechanism of decoupling between mantle flow and lithosphere beneath the EAR is anisotropic viscosity in the asthenosphere. Recent studies on viscous anisotropy in the asthenosphere reveal that the development of olivine aggregates' LPO can weaken the viscosity in the direction parallel to the fabrics and strengthen the viscosity in the perpendicular direction (Hansen et al., 2016; Király et al., 2020). The anisotropic viscosity has important implications for plate motion because it can increase plate velocity in the direction of the LPOs and slow down in the perpendicular direction over a period of up to ∼10 Myr (Király et al., 2020). Moreover, Perry-Houts and KarlstromHere (2019) found that in the lithosphere, the magnitude of anisotropic viscosity is highly dependent on the ratio of intrusion to host rock viscosity, highlighting the importance of anisotropic viscosity in lithospheric deformation modeling. Here, we found that the observed rift parallel NE seismic anisotropy beneath the EAR can be associated with the northward mantle flow from the African Superplume. The presence of such long-term northward flow and the induced LPO could lead to anisotropic viscosity beneath the EAR. This would result in weak viscosity parallel to the rifts and thus faster northward flow than estimated in this study. Conversely, the viscosity in the E-W direction would be stronger causing more resistance to plate motion and would result in slower Somalian plate motion. Since in this study, we have posteriorly calculated the synthetic LPO after the mantle flow simulation, the anisotropic viscosity is not captured in our models. The implementation of anisotropic viscosity would require using a viscosity tensor (e.g., Hansen et al., 2016; Király et al., 2020; Perry-Houts and Karlstrom, 2019) rather than the scalar composite viscosity used here. The concept of anisotropic viscosity beneath the EAR provides new insight into the lithosphere and mantle dynamics beneath East Africa and a future direction for studies of continental rifting.

5 Conclusions

We use 3D thermomechanical modeling of the lithosphere-asthenosphere system to investigate: 1) the role plume-lithosphere interactions beneath the EAR in driving observed surface deformation and 2) the sources of observed seismic anisotropy beneath the EAR oriented approximately ~N-S. We test two types of mantle flow models including a multiple plume model constrained by shear wave tomography from Emry et al. (2019) and an African superplume model simulating a northward mantle wind on the multiple plume model. Our results indicate that interactions of the northward African superplume with the rigid Tanzania Craton, Congo Craton, and Bangweulu and Masai Blocks may be controlling mantle flow pattern beneath the EAR and may be the source of most of the observed seismic anisotropy. We also found that the multiple plume mantle flow model should be ruled out as a dominant source mechanism of sub-lithospheric horizontal mantle flow beneath the EAR. Comparison of dynamic velocities and block kinematics suggests that the Victoria and Rovuma Blocks rotate independently from mantle flow driven by multiple plumes or a superplume. In contrast, we found that for the multiple plumes and superplume mantle flow models, the Somalian plate is over-predicted up to twice or three times its expected rotation rate. While the multiple plumes mantle flow model does not significantly affect the surface deformation driven by the lithospheric buoyancy forces, the northward mantle flow field from the superplume model drives northward component of motions in the deforming zones that improves the fit at the Main Ethiopian Rift, Central Eastern Branch, and northern Western Branch. Those results suggest that sublithospheric viscosity beneath the EAR might be anisotropic due to developed olivine aggregates's LPO induced by the African superplume. The anisotropic viscosity might control the rotation rate of the Somalian Plate.

Acknowledgments

This work was funded by the National Science Foundation (NSF) GeoPRISMS grant EAR-1551864. We used the software Generic Mapping Tools v6.1 (Wessel et al., 2013) to create most of the figures in this paper, except one figure in 3-dimentional that was created using the VISIT v2.9 software developed by the Lawrence Livermore National Laboratory. The ASPECT files needed to reproduce the model is achieved in Zenodo (Rajaonarison et al., 2020b) . In addition, the model output files will be archived at the Open Source Framework repository. We thank the Computational Infrastructure for Geodynamics (CIG) for supporting the development of ASPECT, which is funded by NSF Awards EAR-0949446 and EAR-1550901.

References

J. Albaric, J. Deverchere, J. Perrot, A. Jakovlev, and A. Deschamps. Deep crustal earthquakes in north tanzania, east africa: Interplay between tectonic and magmatic processes in an incipient rift. Geochemistry, Geophysics, Geosystems, 15(2):374–394, 2014.

L. R. Alejano and A. Bobet. Drucker–prager criterion. In The ISRM Suggested Methods for Rock Characterization, Testing and Monitoring: 2007-2014, pages 247–252. Springer, 2012.

C. Amante and B. W. Eakins. Etopo1 arc-minute global relief model: procedures, data sources and analysis. 2009.

J. Austermann, J. X. Mitrovica, P. Huybers, and A. Rovere. Detection of a dynamic topography signal in last interglacial sea-level records. Science Advances, 3(7):e1700457, 2017. doi: 10.1126/sciadv.1700457. URL http://advances.sciencemag.org/lookup/doi/10.1126/sciadv.1700457.

B. Bagley and A. A. Nyblade. Seismic anisotropy in eastern africa, mantle flow, and the african superplume. Geophysical Research Letters, 40(8):1500–1505, 2013.

W. Bangerth, T. Heister, et al. Aspect: Advanced solver for problems in earth's convection. Computational Infrastructure for Geodynamics, 2015.

W. Bangerth, J. Dannberg, R. Gassmoeller, and T. Heister. Aspect v2.2.0, June 2020. URL https://doi.org/10.5281/zenodo.3924604.

I. Bastow, A. A. Nyblade, G. Stuart, T. Rooney, and M. Benoit. Upper mantle seismic structure beneath the ethiopian hot spot: Rifting at the edge of the african low-velocity anomaly. Geochemistry, Geophysics, Geosystems, 9(12), 2008.

T. W. Becker, J. B. Kellogg, G. Ekström, and R. J. O'Connell. Comparison of azimuthal seismic anisotropy from surface waves and finite strain from global mantle-circulation models. Geophysical Journal International, 155(2):696–714, 2003.

T. W. Becker, S. Chevrot, V. Schulte-Pelkum, and D. K. Blackman. Statistical properties of seismic anisotropy predicted by upper mantle geodynamic models. Journal of Geophysical Research: Solid Earth, 111(B8), 2006.

Becker, T. W. (2006). On the effect of temperature and strain-rate dependent viscosity on global mantle flow, net rotation, and plate-driving forces. Geophysical Journal International, 167(2), 943-957.

T. W. Becker, C. P. Conrad, A. J. Schaeffer, and S. Lebedev. Origin of azimuthal seismic anisotropy in oceanic plates and mantle. Earth and Planetary Science Letters, 401:236–250, 2014.

M. H. Benoit, A. A. Nyblade, and J. C. VanDecar. Upper mantle p-wave speed variations beneath ethiopia and the origin of the afar hotspot. Geology, 34(5):329–332, 2006.

Bott, M. H. P., & Kusznir, N. J. (1979). Stress distributions associated with compensated plateau uplift structures with application to the continental splitting mechanism. *Geophysical Journal International*, *56*(3), 451-459.

Brune, S. (2018). Forces within continental and oceanic rifts: Numerical modeling elucidates the impact of asthenospheric flow on surface stress. *Geology*, *46*(2), 191-192.

Buck, W. R. (1991). Modes of continental lithospheric extension. *Journal of Geophysical Research: Solid Earth*, *96*(B12), 20161-20178.

Bird, P., Liu, Z., & Rucker, W. K. (2008). Stresses that drive the plates from below: Definitions, computational path, model optimization, and error analysis. *Journal of Geophysical Research: Solid Earth*, *113*(B11).

V. E. Camp and M. J. Roobol. Upwelling asthenosphere beneath western arabia and its regional implications. Journal of Geophysical Research: Solid Earth, 97(B11):15255–15271, 1992.

S.-J. Chang and S. Van der Lee. Mantle plumes and associated flow beneath arabia and east africa. Earth and Planetary Science Letters, 302(3-4):448–454, 2011.

Chang, S. J., Kendall, E., Davaille, A., & Ferreira, A. M. (2020). The evolution of mantle plumes in East Africa. *Journal of Geophysical Research: Solid Earth*, *125*(12), e2020JB019929.

D. Chapman. Thermal gradients in the continental crust. Geological Society, London, Special Publications, 24(1):63–70, 1986.

D. D. Coblentz and M. Sandiford. Tectonic stresses in the african plate: Constraints on the ambient lithospheric stress state. Geology, 22(9):831–834, 1994.

C. P. Conrad and C. Lithgow-Bertelloni. Influence of continental roots and asthenosphere on plate-mantle coupling. Geophysical Research Letters, 33(5), 2006.

Conrad, C. P., & Behn, M. D. (2010). Constraints on lithosphere net rotation and asthenospheric viscosity from global mantle flow models and seismic anisotropy. Geochemistry, Geophysics, Geosystems, 11(5).

A. Dziewonski, T.-A. Chou, and J. H. Woodhouse. Determination of earthquake source parameters from waveform data for studies of global and regional seismicity. Journal of Geophysical Research: Solid Earth, 86(B4):2825–2852, 1981.

C. J. Ebinger and N. Sleep. Cenozoic magmatism throughout east africa resulting from impact of a single plume. Nature, 395(6704):788–791, 1998.

G. Ekström, M. Nettles, and A. Dziewoński. The global cmt project 2004–2010: Centroidmoment tensors for 13,017 earthquakes. Physics of the Earth and Planetary Interiors, 200:1–9, 2012.

E. L. Emry, Y. Shen, A. A. Nyblade, A. Flinders, and X. Bao. Upper mantle earth structure in africa from full-wave ambient noise tomography. Geochemistry, Geophysics, Geosystems, 20(1):120–147, 2019.

M. Faccenda and F. Capitanio. Development of mantle seismic anisotropy during subduction induced 3-D flow. Geophysical Research Letters, 39(11), 2012.

M. Faccenda and F. A. Capitanio. Seismic anisotropy around subduction zones: Insights from three-dimensional modeling of upper mantle deformation and sks splitting calculations. Geochemistry, Geophysics, Geosystems, 14(1):243–262, 2013.

S. Fishwick. Surface wave tomography: imaging of the lithosphere–asthenosphere boundary beneath central and southern Africa? Lithos, 120(1):63–73, 2010, updated.

Froidevaux, C., & Nataf, H. C. (1981). Continental drift: What driving mechanism?. *Geologische Rundschau*, *70*(1), 166-176.

A. M. Forte, S. Quéré, R. Moucha, N. A. Simmons, S. P. Grand, J. X. Mitrovica, and D. B. Rowley. Joint seismic–geodynamic-mineral physical modelling of african geodynamics: A reconciliation of deep-mantle convection with surface geophysical constraints. Earth and Planetary Science Letters, 295(3-4):329–341, 2010.

T. Furman, J. Bryce, T. Rooney, B. Hanan, G. Yirgu, and D. Ayalew. Heads and tails: 30 million years of the afar plume. Geological Society, London, Special Publications, 259(1): 95–119, 2006.

S. Gao, P. M. Davis, H. Liu, P. D. Slack, A. W. Rigor, Y. A. Zorin, V. V. Mordvinova, V. M. Kozhevnikov, and N. A. Logatchev. Sks splitting beneath continental rift zones. Journal of Geophysical Research: Solid Earth, 102(B10):22781–22797, 1997.

R. George, N. Rogers, and S. Kelley. Earliest magmatism in ethiopia: evidence for two mantle plumes in one flood basalt province. Geology, 26(10):923–926, 1998.

A. Ghosh and W. E. Holt. Plate motions and stresses from global dynamic models. Science, 335(6070):838–843, 2012.

A. Glerum, C. Thieulot, M. Fraters, C. Blom, and W. Spakman. Nonlinear viscoplasticity in aspect: benchmarking and applications to subduction. Solid Earth, 9:267–294, 2018.

Glerum, A., Brune, S., Stamps, D. S., & Strecker, M. R. (2020). Victoria continental microplate dynamics controlled by the lithospheric strength distribution of the East African Rift. *Nature communications*, *11*(1), 1-15.

Ghosh, A., & Holt, W. E. (2012). Plate motions and stresses from global dynamic models. *Science*, *335*(6070), 838-843.

L. N. Hansen, J. M. Warren, M. E. Zimmerman, and D. L. Kohlstedt. Viscous anisotropy of textured olivine aggregates, part 1: Measurement of the magnitude and evolution of anisotropy. Earth and Planetary Science Letters, 445:92–103, 2016.

S. E. Hansen, A. A. Nyblade, and M. H. Benoit. Mantle structure beneath africa and arabia from adaptively parameterized p-wave tomography: Implications for the origin of cenozoic afro-arabian tectonism. Earth and Planetary Science Letters, 319:23–34, 2012.

G. Helffrich. Lithospheric deformation inferred from teleseismic shear wave splitting observations in the United kingdom. Journal of Geophysical Research: Solid Earth, 100(B9): 18195–18204, 1995.

G. Hirth and D. Kohlstedt. Rheology of the upper mantle and the mantle wedge: A view from the experimentalists. Inside the Subduction Factory, pages 83–105, 2003.

B. Homuth, U. Löbl, A. Batte, K. Link, C. Kasereka, and G. Rümpker. Seismic anisotropy of the lithosphere/asthenosphere system beneath the rwenzori region of the albertine rift. International Journal of Earth Sciences, 105(6):1681–1692, 2016.

J. Hu, M. Faccenda, and L. Liu. Subduction-controlled mantle flow and seismic anisotropy in South America. Earth and Planetary Science Letters, 470:13–24, 2017.

M. A. Jadamec and M. I. Billen. Reconciling surface plate motions with rapid threedimensional mantle flow around a slab edge. Nature, 465(7296):338, 2010.

E. Kaminski and N. Ribe. A kinematic model for recrystallization and texture development in olivine polycrystals. Earth and Planetary Science Letters, 189(3):253–267, 2001.

E. Kaminski and N. M. Ribe. Timescales for the evolution of seismic anisotropy in mantle flow. Geochemistry, Geophysics, Geosystems, 3(8):1–17, 2002.

E. Kaminski, N. M. Ribe, and J. T. Browaeys. D-Rex, a program for calculation of seismic anisotropy due to crystal lattice preferred orientation in the convective upper mantle. Geophysical Journal International, 158(2):744–752, 2004.

S.-i. Karato. Importance of anelasticity in the interpretation of seismic tomography. Geophysical Research Letters, 20(15):1623–1626, 1993.

J.-M. Kendall and C. Lithgow-Bertelloni. Why is Africa rifting? Geological Society, London, Special Publications, 420(1):11–30, 2016.

Á. Király, C. P. Conrad, and L. N. Hansen. Evolving viscous anisotropy in the upper mantle and its geodynamic implications. Geochemistry, Geophysics, Geosystems, 21(10): e2020GC009159, 2020.

Koptev, A., Burov, E., Calais, E., Leroy, S., Gerya, T., Guillou-Frottier, L., & Cloetingh, S. (2016). Contrasted continental rifting via plume-craton interaction: Applications to Central East African Rift. Geoscience Frontiers, 7, 221–236. https://doi.org/10.1016/j.gsf.2015.11.002

Koptev, A., Burov, E., Gerya, T., Le Pourhiet, L., Leroy, S., Calais, E., & Jolivet, L. (2018a). Plume-induced continental rifting and breakup in ultra-slow extension context: Insights from 3D numerical modeling. Tectonophysics, 746, 121–137. https://doi.org/10.1016/j.tecto.2017.03.025

Koptev, A., Calais, E., Burov, E., Leroy, S., & Gerya, T. (2018b). Along-axis variations of rift width in a coupled lithosphere-mantle system, application to East Africa. Geophysical Research Letters, 45, 5362–5370. https://doi.org/10.1029/2018GL077276

Koptev, A., Cloetingh, S., Gerya, T., Calais, E., & Leroy, S. (2018c). Non-uniform splitting of a single mantle plume by double cratonic roots: Insight into the origin of the central and southern East African rift system. Terra Nova, 30, 125–134. https://doi.org/10.1111/ter.12317

M. Kronbichler, T. Heister, and W. Bangerth. High accuracy mantle convection simulation through modern numerical methods. Geophysical Journal International, 191(1):12–29, 2012.

G. Laske, Z. Ma, G. Masters, and M. Pasyanos. Crust 1.0: a new global crustal model at 1Å~ 1 degrees, 2013.

Lithgow-Bertelloni, C., & Guynn, J. H. (2004). Origin of the lithospheric stress field. *Journal of Geophysical Research: Solid Earth*, *109*(B1).

Lithgow-Bertelloni, C., & Silver, P. G. (1998). Dynamic topography, plate driving forces and the African superswell. *Nature*, *395*(6699), 269-272.

R. Montelli, G. Nolet, F. Dahlen, and G. Masters. A catalog of deep mantle plumes: New results from finite-frequency tomography. Geochemistry, Geophysics, Geosystems, 7(11), 2006.

Mulugeta, G. (1985). Dynamic models of continental rift valley systems. *Tectonophysics*, *113*(1-2), 49-73.

Naliboff, J. B., Glerum, A., Brune, S., Péron-Pinvidic, G., & Wrona, T. (2020). Development of 3-D rift heterogeneity through fault network evolution. *Geophysical Research Letters*, *47*(13), e2019GL086611.

E. A. Njinju, F. Kolawole, E. A. Atekwana, D. S. Stamps, E. A. Atekwana, M. G. Abdelsalam, and K. L. Mickus. Terrestrial heat flow in the malawi rifted zone, east africa: Implications for tectono-thermal inheritance in continental rift basins. Journal of Volcanology and Geothermal Research, 387:106656, 2019b.

E. A. Njinju, Stamps, D. S., Neumiller, K., & Gallager, J. (2021). Lithospheric control of melt generation beneath the Rungwe Volcanic Province, East Africa: Implications for a plume source. Journal of Geophysical Research: Solid Earth, 126(5), e2020JB020728.

A. A. Nyblade. Heat flow and the structure of Precambrian lithosphere. In Developments in Geotectonics, volume 24, pages 81–91. Elsevier, 1999.

A. A. Nyblade and S. W. Robinson. The african superswell. Geophysical research letters, 21 (9):765–768, 1994.

T. J. O. H. G. J. R. Nyblade, A. and C. A. Langston. Seismic evidence for a deep upper mantle thermal anomaly beneath East Africa, 2000.

M. E. Pasyanos. A lithospheric attenuation model of North America, 2013.

J. Perry-Houts and L. Karlstrom. Anisotropic viscosity and time-evolving lithospheric instabilities due to aligned igneous intrusions. Geophysical Journal International, 216(2): 794–802, 2019.

T. A. Rajaonarison, D. S. Stamps, S. Fishwick, S. Brune, A. Glerum, and J. Hu. Numerical modeling of mantle flow beneath madagascar to constrain upper mantle rheology beneath continental regions. Journal of Geophysical Research. Solid Earth, 125(2):Art–No, 2020.

N. M. Ribe and Y. Yu. A theory for plastic deformation and textural evolution of olivine polycrystals. Journal of Geophysical Research: Solid Earth, 96(B5):8325–8335, 1991.

J. Ritsema, H. J. van Heijst, and J. H. Woodhouse. Complex shear wave velocity structure imaged beneath africa and iceland. Science, 286(5446):1925–1928, 1999.

T. O. Rooney, C. Herzberg, and I. D. Bastow. Elevated mantle temperature beneath east africa. Geology, 40(1):27–30, 2012.

E. Saria, E. Calais, D. Stamps, D. Delvaux, and C. Hartnady. Present-day kinematics of the east african rift. Journal of Geophysical Research: Solid Earth, 119(4):3584–3600, 2014.

B. Schuberth, H.-P. Bunge, G. Steinle-Neumann, C. Moder, and J. Oeser. Thermal versus elastic heterogeneity in high-resolution mantle circulation models with pyrolite composition: High plume excess temperatures in the lowermost mantle. Geochemistry, Geophysics, Geosystems, 10(1), 2009.

N. A. Simmons, A. M. Forte, and S. P. Grand. Thermochemical structure and dynamics of the african superplume. Geophysical Research Letters, 34(2), 2007.

N. A. Simmons, A. M. Forte, and S. P. Grand. Joint seismic, geodynamic and mineral physical constraints on three-dimensional mantle heterogeneity: Implications for the relative importance of thermal versus compositional heterogeneity. Geophysical Journal International, 177(3):1284–1304, 2009.

D. Stamps, L. Flesch, E. Calais, and A. Ghosh. Current kinematics and dynamics of africa and the east african rift system. Journal of Geophysical Research: Solid Earth, 119(6): 5161–5186, 2014.

D. Stamps, G. Iaffaldano, and E. Calais. Role of mantle flow in nubia-somalia plate divergence. Geophysical Research Letters, 42(2):290–296, 2015.

D. Stamps, C. Kreemer, R. Fernandes, T. Rajaonarison, and G. Rambolamanana. Redefining east african rift system kinematics. Geology, 2020.

D. S. Stamps, E. Saria, and C. Kreemer. A geodetic strain rate model for the east african rift system. Scientific reports, 8(1):1–8, 2018.

P. R. Stoddard and D. Abbott. Influence of the tectosphere upon plate motion. Journal of

Geophysical Research: Solid Earth, 101(B3):5425–5433, 1996.

K. T. Walker, A. A. Nyblade, S. L. Klemperer, G. H. Bokelmann, and T. J. Owens. On the relationship between extension and anisotropy: Constraints from shear wave splitting across the east african plateau. Journal of Geophysical Research: Solid Earth, 109(B8), 2004.

S. Zhong. Role of ocean-continent contrast and continental keels on plate motion, net rotation of lithosphere, and the geoid. Journal of Geophysical Research: Solid Earth, 106(B1):703–712, 2001.

Table 1: A comparison of TI-axis, or synthetic LPO, from the two models (multiple plumes and superplume) produced in this work with observed anisotropy. $<\phi_{obs}>$ and $<\delta t_{obs}>$ are the observed regional mean fast direction, respectively. TI-axis represents the predicted synthetic LPO. $<\Delta\alpha>$ is the regional mean angular misfit between the observed fast direction and predicted LPO.

	Observations		Multiple Plumes Model				Superplume Model			
Region	$<\phi_{obs}>^\circ$	$<\delta t_{obs}>$ (s)	TI-axis		$<\Delta\alpha>^\circ$		TI-axis		$<\Delta\alpha>^\circ$	
Depth	-	-	150 km	300 km	150 km	300 km	150 km	300 km	150 km	300 km
Northern	N27°E	1.3	S20°E	S20°E	51°	51°	S30°E	N23°E	60°	20°
Center	N26°E	1.	S15°E	S20°E	52°	51°	S1°E	N13°E	44°	27°
South	N35°E	0.8	N20°E	N1°E	40°	46°	N20°E	N56°E	46°	40°

Table 2: Summary of the comparison of dynamic velocities from this study (driven by GPE + Multiple Plumes Model and GPE + Superplume Model) and from Rajaonarison et al. (under review, GRL) (driven by GPE only) with kinematic model from Stamps et al. (2020) and GNSS/GPS velocities from Stamps et al. (2018) in deforming zones defined as regions A-F. V (mm/yr) represents mean velocity, α represents mean angular misfit ([0 - 180◦] from good to poor fit), and RMS is the root mean square velocity.

	Kinematic model/GPS	GPE only			GPE+Multiple Plumes Model			GPE+Superplume Model		
Region	$\overline{V}(mm/yr)$	$\overline{V}(mm/yr)$	RMS (mm/yr)	α	$\overline{V}(mm/yr)$	RMS (mm/yr)	α	$\overline{V}$	RMS (mm/yr)	α
Somalian Plate	4.41	6	1.8	10°	13	12.	5°	7.5	5.	5°
Victoria Block	2.13	1.39	0.5	5°	2.5	0.5	6°	2.8	0.6	7°
Rovuma Block	2.14	2.3	0.2	10°	2.	0.5	10°	3.1	1.	6°
Region A	2.59	5.9	2.6	66°	7.1	6	60°	8.1	6.	50°
Region B	2.7	4.3	1.6	12°	2.7	2.1	5°	2.7	0.7	40°
Region C	3.2	5.1	1.3	74°	2.9	2.5	50°	2.7	1.8	3°
Region D	2.8	3.2	1.1	8°	2.	1.5	4°	2.	1.8	30°
Region E	2.55	0.54	1.9	114 °	0.2	1.36	99°	0.3	1.3	4°
Region F	2.6	1.9	0.8	20°	2.4	0.8	20°	2.9	0.7	24°

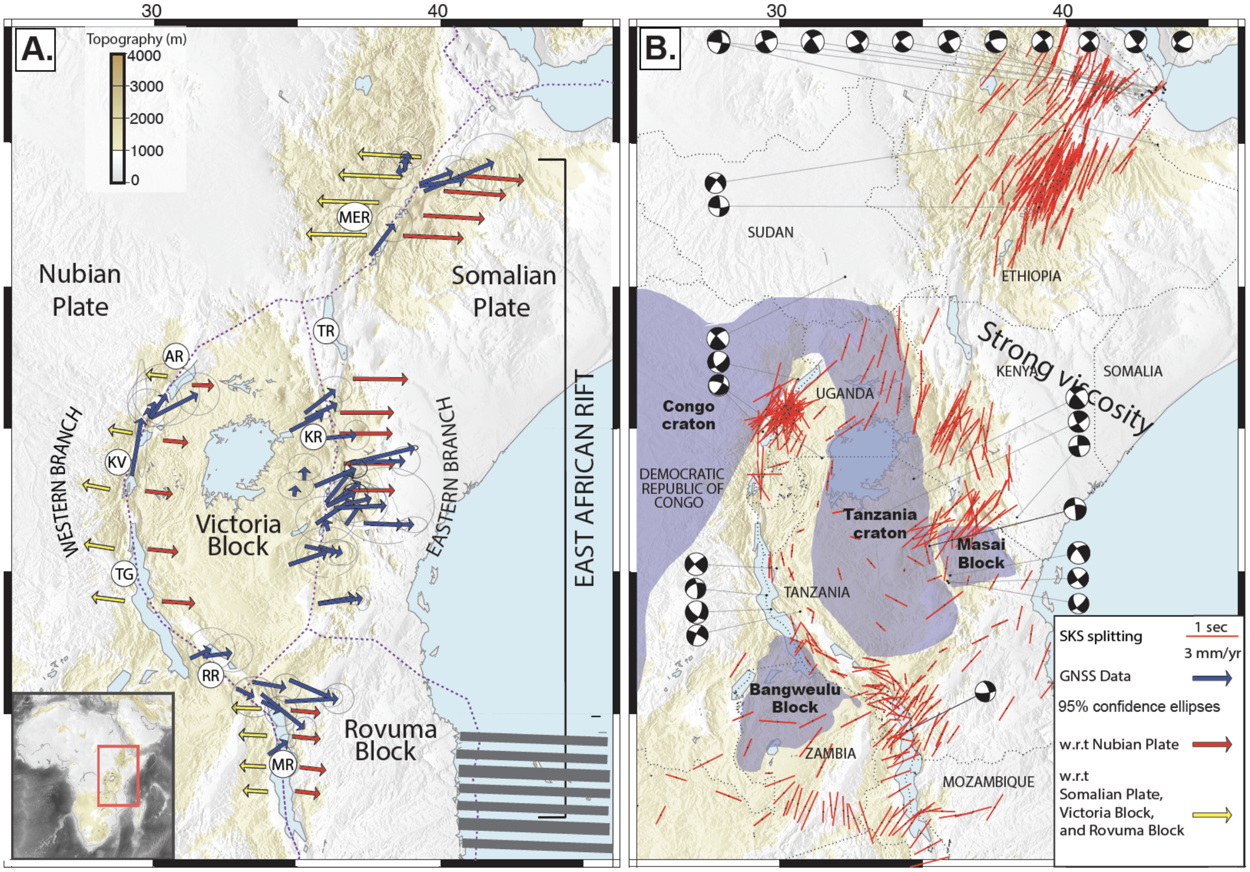

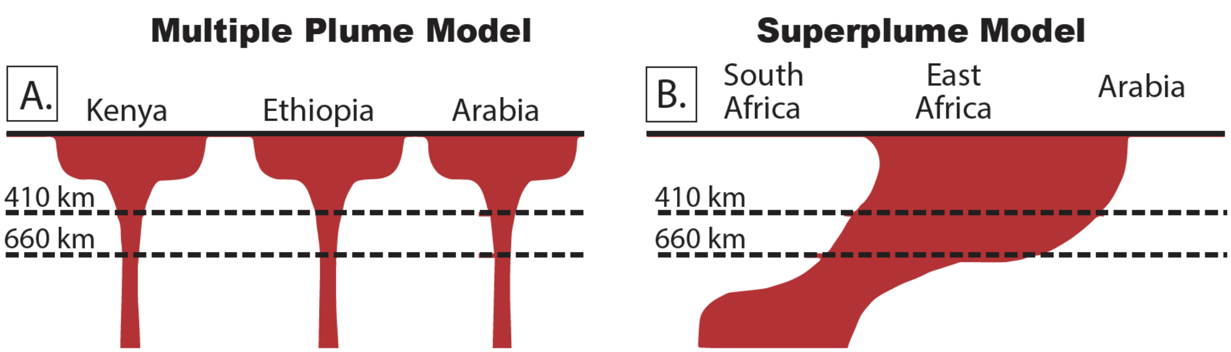

Figure 1: A) GPS velocities along the deforming zone of the East African Rift (EAR; Stamps et al., 2018; blue vectors with 95% confidence ellipses). Red and yellow vectors are kinematic models from Saria et al. (2014) for the Somalian Plate, the Victoria Block, and the Rovuma Block, respectively. Purple dashed lines are plate boundaries. B) Observed SKS splitting (blue bars) and strike-slip focal mechanisms along the EAR. Several rifts are defined: TG = Tanganyika Rift, RR = Rukwa Rift, AR = Albertine Rift, MER = Main Ethiopian Rift, TR = Turkana Rift, KR = Kenya

Rift, MR = Malawi Rift, and KV = Kivu Rift. Black dots indicate earthquake locations where strike-slip focal mechanisms are observed (GCMT; Dziewonski et al., 1981; Ekström et al., 2012). Dashed lines are political boundaries. Hashed lines indicate deforming zones from Stamps et al. (2020). (C and D) Plume models for the East African Rift System invoked to explain upper mantle seismic velocity models (adapted from Hansen et al., 2012). C) The multiple plume model. D) The superplume model that is referred to as African superplume.

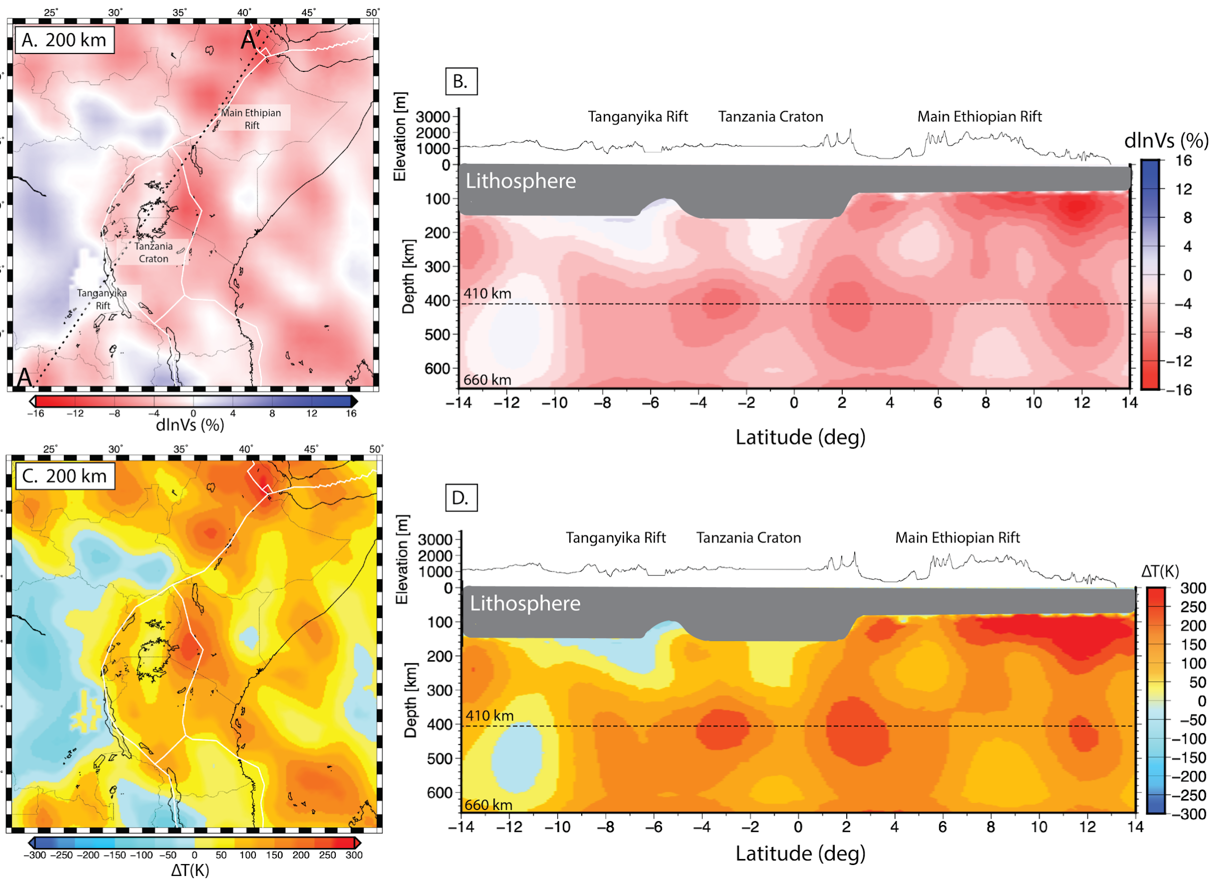

Figure 2: (A,B) Shear wave tomography anomaly from Emry et al. (2019): A) at 200 km depth and B) along profile AA′. (C,D) Temperature anomaly obtained by converting the shear wave tomography in A and B. C) at 200 km depth and D) along profile AA′).

879

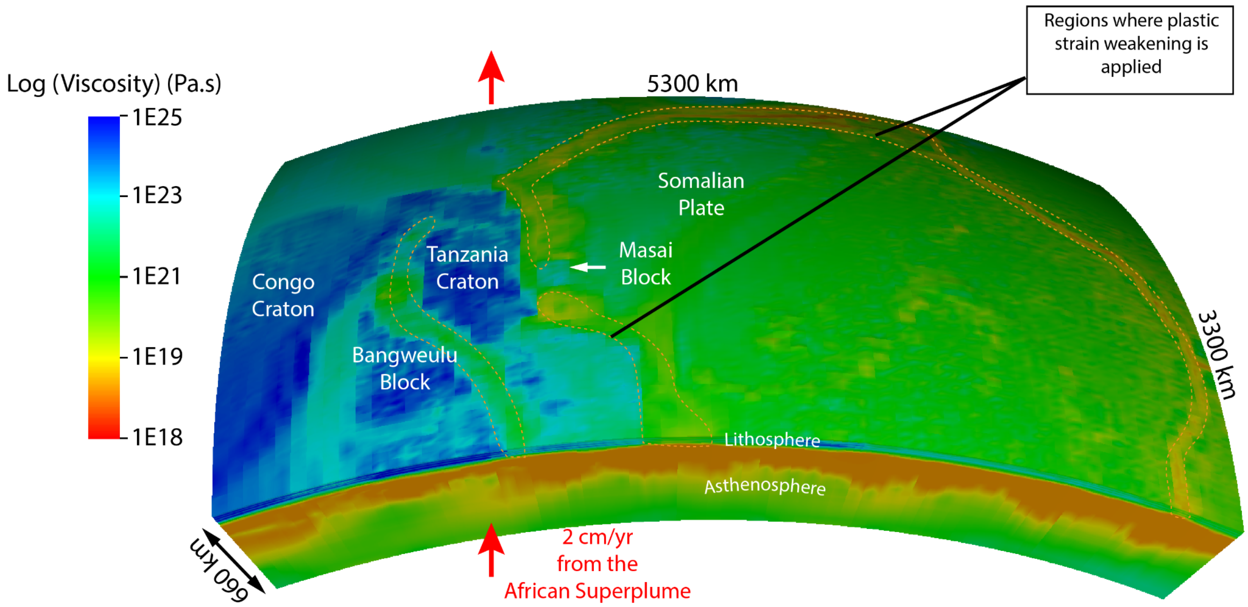

880 **Figure 3:** 3D viscosity model used in this study. Dashed orange lines indicate regions where a

881 plastic weakening mechanism is applied to localize deformation. Red vectors indicate the

882 velocity boundary condition used to simulate the African Superplume.

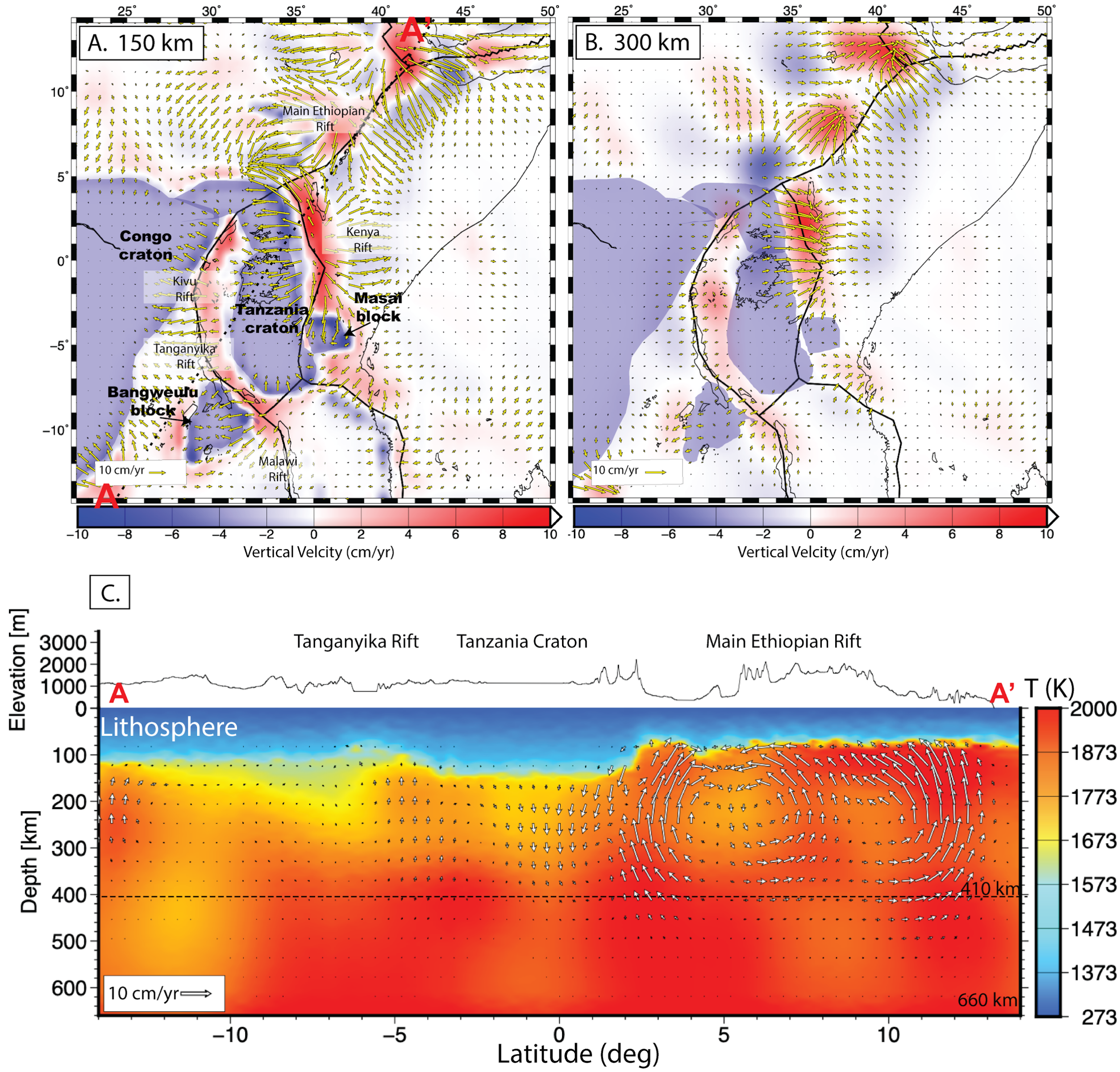

Figure 4: Mantle flow field from the multiple plumes model: A) at 150 km depth, B) at 300 km depth. Background color indicates vertical flow. Yellow vectors portray horizontal. C) along profile AA′ (Figure 4A). The background color indicates the temperature field.

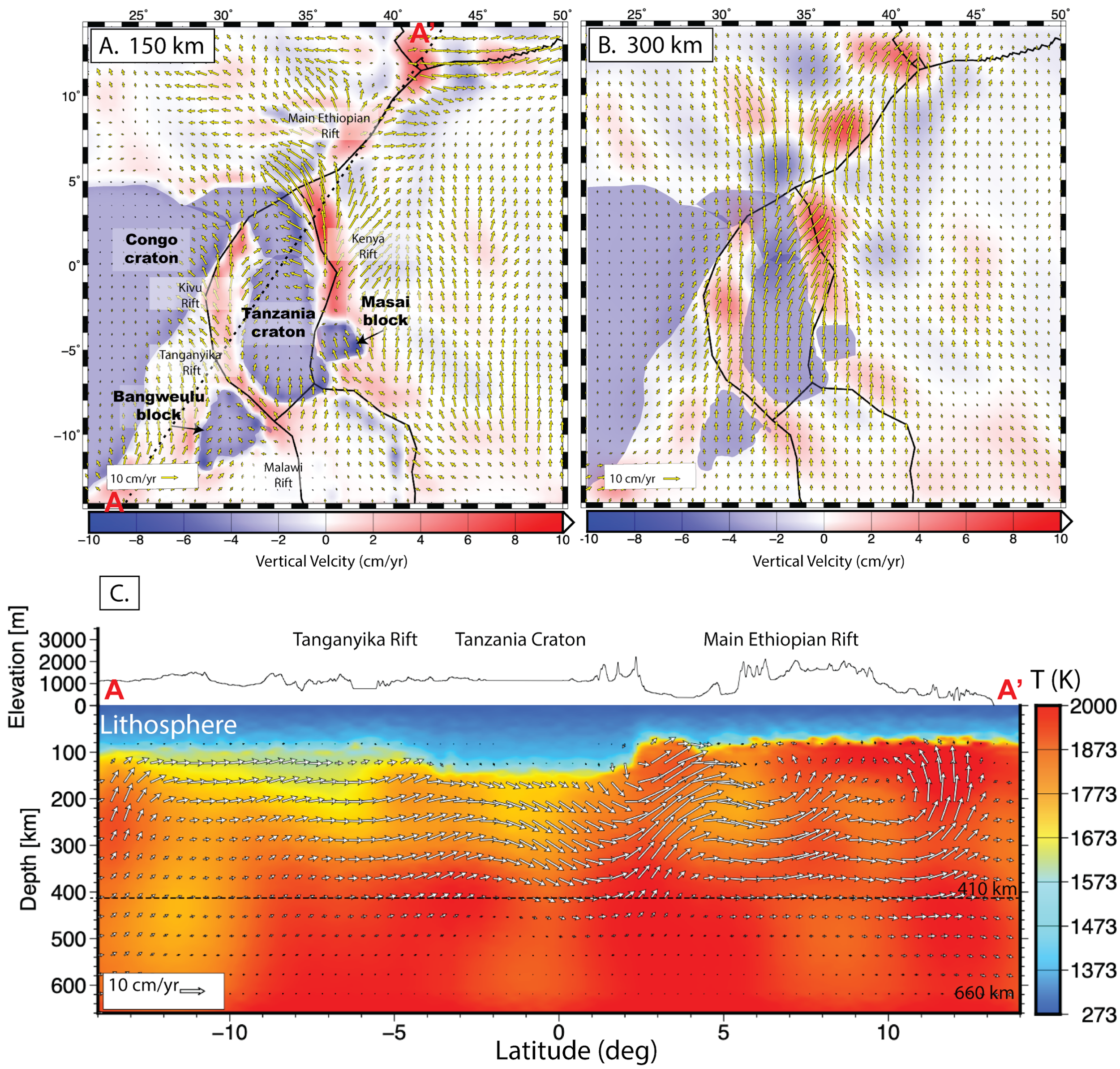

Figure 5: Mantle flow field from the superplume model: A) at 150 km depth, B) at 300 km depth. Background color indicates vertical flow. Yellow vectors portray horizontal. C) along profile AA′ (Figure 5A). The background color indicates the temperature field.

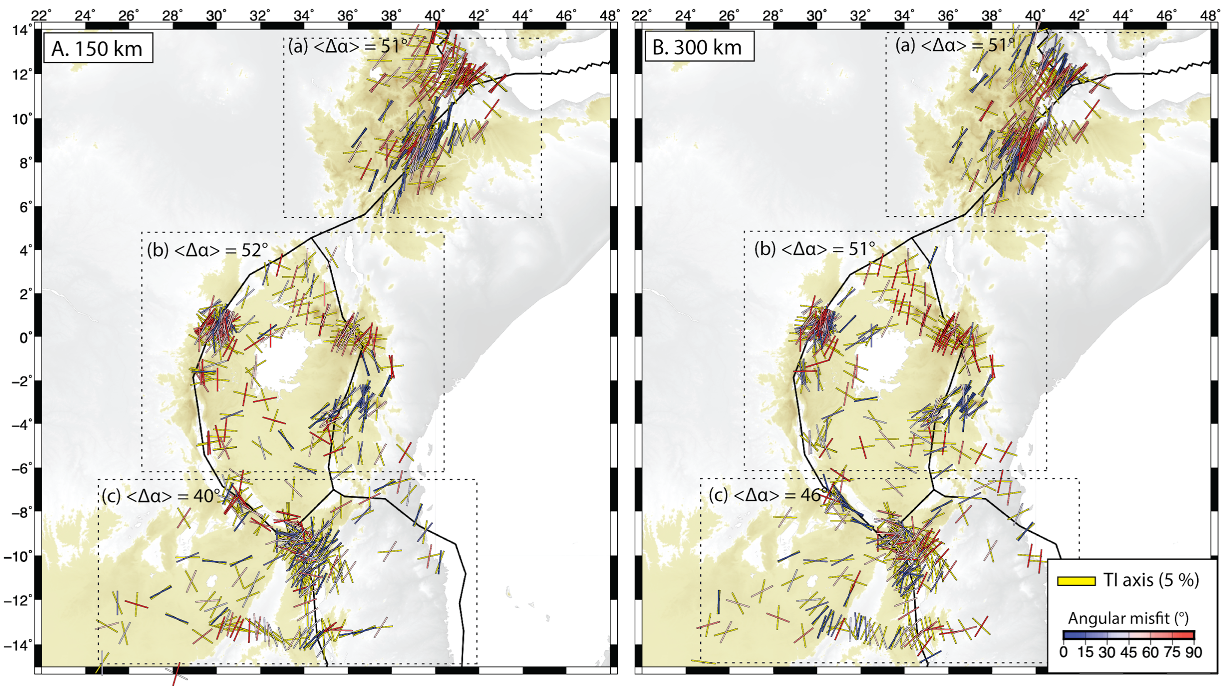

Figure 6: Comparison of calculated TI axes with observations from the multiple plume model: A) at 150 km and B) at 300 km. The yellow bars indicate TI axis orientation. The SKS splitting measurement bars are colored according to angular misfit [0° - 90°]. The background shows topography.

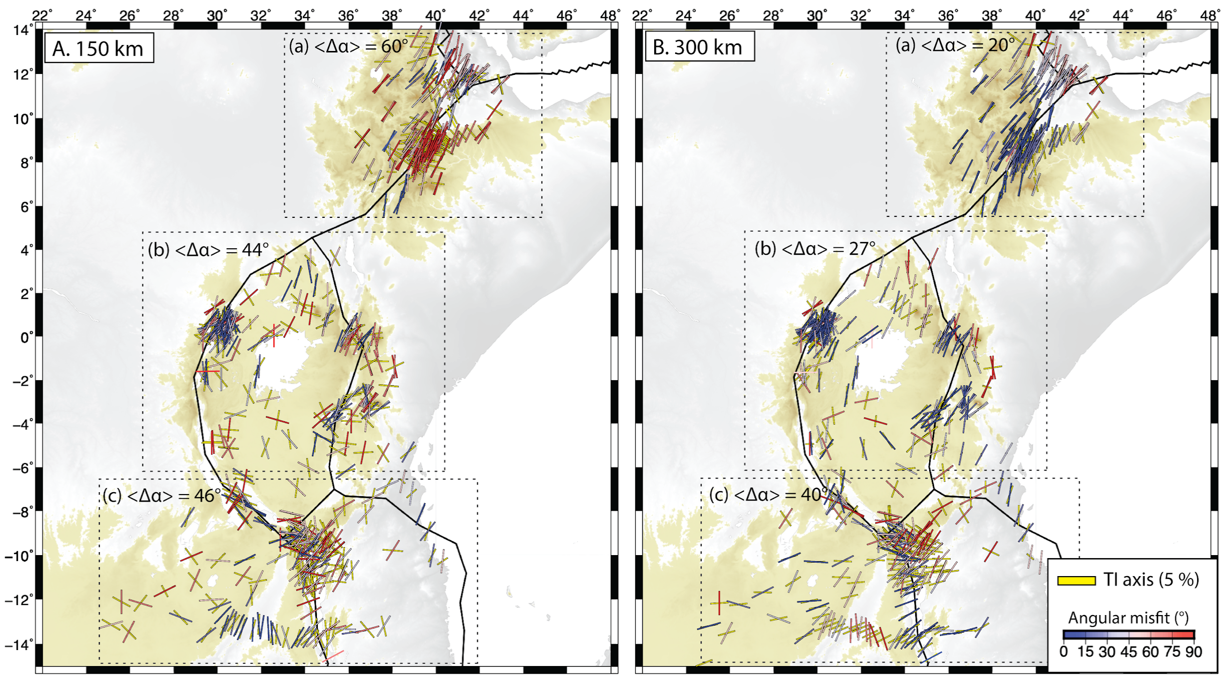

Figure 7: Comparison of calculated TI axes with observations from the superplume model: A) at 150 km and B) at 300 km. The yellow bars indicate TI axis orientation. The SKS splitting measurement bars are colored according to angular misfit [0°- 90°]. The background shows topography.

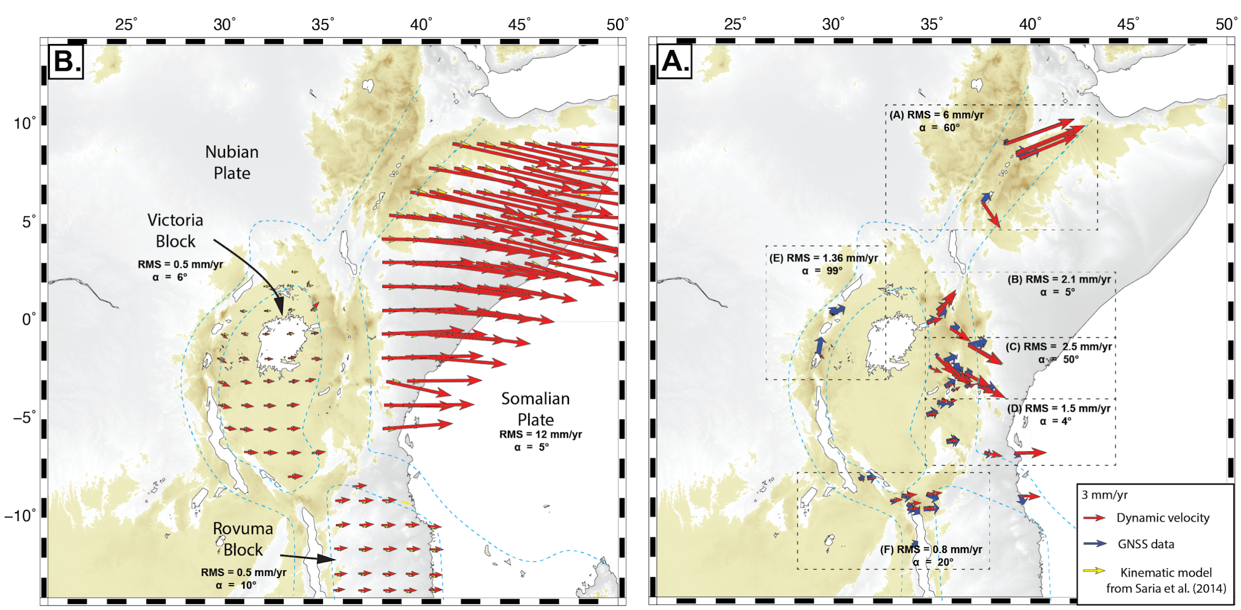

Figure 8: Comparison of dynamic velocities (red vectors) driven by mantle tractions from the multiple plumes model and lithospheric buoyancy forces with: A) kinematic predictions from the Stamps et al. (2021) model (yellow vectors) within the Somalian Plate, the Victoria and the Rovuma Blocks. B) GNSS/GPS data from (Stamps et al., 2018, blue vectors) within the deforming zones (dashed blue line) and comparisons statistics (RMS and mean angular misfit) are shown inside a dashed box for each region.

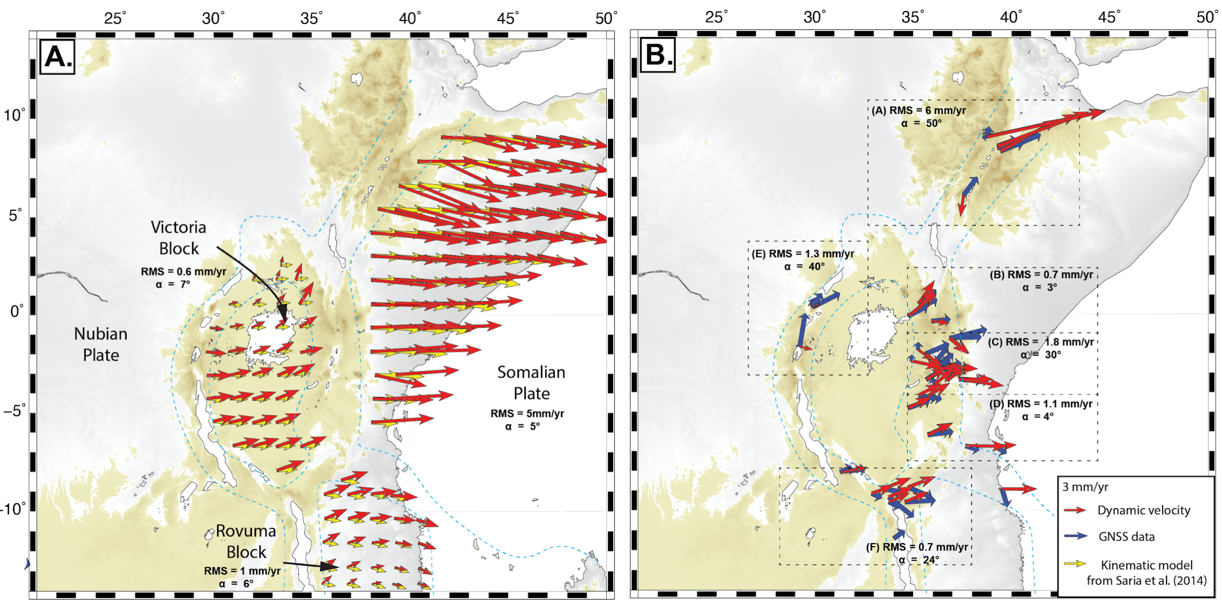

Figure 9: Comparison of dynamic velocities (red vectors) driven by mantle tractions from the superplume model and lithospheric buoyancy forces with: A) kinematic predictions from the Stamps et al. (2021) model (yellow vectors) within the Somalian Plate, the Victoria and the Rovuma Blocks. B) GNSS/GPS data from (Stamps et al., 2018, blue vectors) within the deforming zones (dashed blue line) and Comparisons statistics (RMS and mean angular misfit) are shown inside a dashed box for each region.